Supplementary Information

A hybrid method combining discharge-assisted laser induced breakdown spectroscopy with wavelet transform for trace elemental analysis in liquid targets

Boping Xu[1,2], Simeng Liu[1,2], Bingying Lei[1,2], Jing Wang[1,2], Yinghua Liu[1,2], Wenfu Zhang[1,2], Jie Tang[1,2,*], Yishan Wang[1,2], Wei Zhao[1,2], and Yixiang Duan[3]

[1]*State Key Laboratory of Transient Optics and Photonics, Xi'an Institute of Optics and Precision Mechanics of CAS, Xi'an 710119, China*

[2]*University of Chinese Academy of Sciences, Beijing 100049, China*

[3]*Key Laboratory of Synthetic and Natural Functional Molecule Chemistry of Ministry of Education, College of Chemistry and Materials Science, Northwest University, Xi'an 710127, China*

*E-mail: tangjie@opt.ac.cn

Table of Contents

A. Measurement of the discharge energy

Figure S1 shows the temporary evolution of discharge voltage and discharge current in the discharge-assisted laser induced breakdown spectroscopy (D-LIBS). When the discharge is triggered by the laser-induced plasmas, the discharge energy is deposited into the plasmas in the whole discharge process, which can be described as equation (1):

$$Q = \int_{t_1}^{t_2} V(t) \cdot I(t)dt + \int_{t_2}^{t_3} V(t) \cdot I(t)dt, \quad (1)$$

where t_1 is the start of discharge at 0 μs, t_2 is the end of oscillation at 10 μs, and t_3 is the end of discharge at 726 μs. Q is the discharge energy. $V(t)$ and $I(t)$ are the voltage and the current, respectively. The first term on the left represents the spark discharge energy in the oscillating zone, and the second term represents the non-oscillating zone. When the laser energy is 50 mJ, the discharge energies deposited into the plasma in the oscillating zone and non-oscillating zone are respectively calculated to be 15.96 mJ and 24.01 mJ. Thus, the total energy introduced into the plasma is 39.97 mJ.

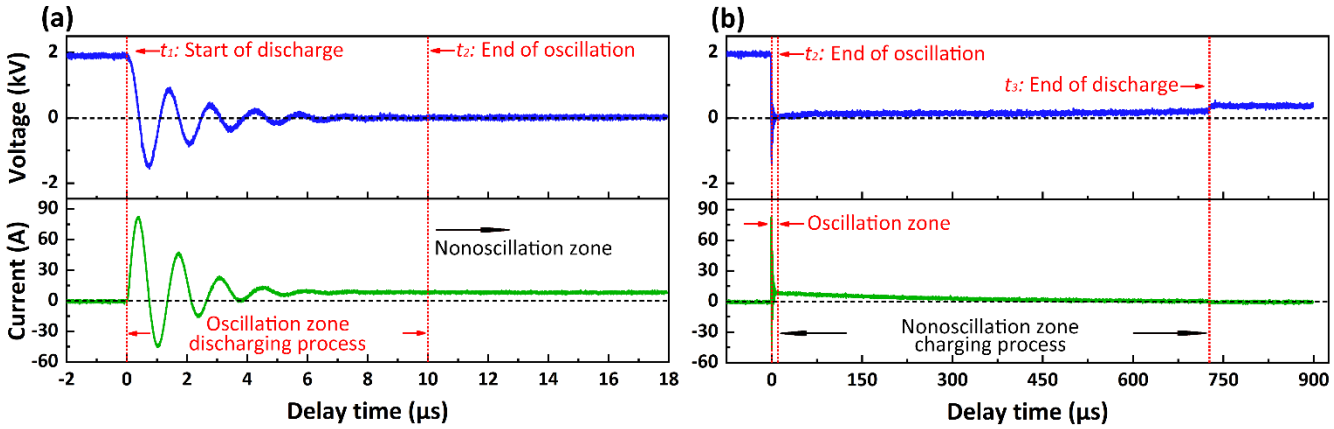

Figure S1. Temporal evolutions of the discharge voltage and discharge current in the time scale of (a) 0–18 μs and in (b) 0–900 μs. t_1=0 μs, t_2=10 μs and t_3=726 μs.

B. Methods

a) Wavelet Transform De-noising

Wavelet transform (WT) is a method of time-frequency analysis of signals. WT decomposes the signal into a series of wavelet functions, which have the characteristics of multi-resolution analysis, compared with Fourier transform (FT). In both local time and frequency domain, WT can characterize the local signal. The basic principle of WT is that the mother wavelet undergoes scaling and shifting transform and then takes the inner product with original signal $f(t)$, as shown in equation (2):

$$\mathrm{WT}(\alpha,\tau) = \frac{1}{\sqrt{\alpha}}\int_{-\infty}^{+\infty} f(t) * \psi\left(\frac{t-\tau}{\alpha}\right) dt, \quad (2)$$

where α and τ are scaling and shifting parameters, respectively. $f(t)$ is original signal and $\psi(t)$ is mother wavelet. In general, the original signal $f(t)$ is composed of a real signal $s(t)$ and a noise signal $n(t)$ and coefficients of wavelet transform $\mathrm{WT}(\alpha,\tau)$ also consist of $s(\alpha,\tau)$ and $n(\alpha,\tau)$, as shown in equations (3) and (4):

$$f(t) = s(t) + n(t), \quad (3)$$

$$\mathrm{WT}(\alpha,\tau) = s(\alpha,\tau)n(\alpha,\tau). \quad (4)$$

While for WT, the mother wavelet, decomposition layer, and noise coefficient threshold have strong influence on the reconstructed signal. Each mother wavelet has its own advantage in signal processing, and there is no one kind of wavelet basis function that can achieve the optimal de-noise effect for all types of signals. Daubechies (db) wavelet[1-3] is often utilized for spectral signal. In WTDN, the decomposition layer is also a very important parameter. The larger the decomposition layer is, the more the difference between the characteristics of noise and signal, and the better the separation between them. On the other hand, the larger the number of decomposition layer is, the greater the distortion of reconstructed signal, which determines the final de-noising. In this work the hard thresholding function is used for signal processing. It means that the noise coefficient located in $[-3\sigma, 3\sigma]$ is set to be zero, where σ is the variance of noise coefficient. Moreover, the mother wavelet and decomposition layer are optimized by evaluating R^2, root mean square error (RMSE), and signal to noise ratio (SNR) of spectra.

b) Partial Least Squares Regression

Partial least squares regression (PLSR), which was developed in the 1980s, is a multivariate data analysis method based on principal component analysis and principal component regression. PLSR associates the data

matrices **X** and data matrices **Y** by multiple iterative calculations, as shown in equation (5):

$$\mathbf{Y} = \mathbf{XW} + \mathbf{E}, \tag{5}$$

where **Y** is the dependent variable matrix of **n** by **m** (**n** samples and **m** variables), **X** is the independent variable matrix of n by p (n samples and p variables); W is the model regression coefficient, and E is the model residual error.

Here, the general principle of PSLR is briefly described following R. Roman et al [4]. PSLR decomposes the independent variable matrix **X** and the dependent variable matrix **Y** according to the following formulas:

$$\mathbf{X} = \mathbf{TP}^{\mathrm{T}} + \mathbf{E}, \tag{6}$$

$$\mathbf{Y} = \mathbf{UQ}^{\mathrm{T}} + \mathbf{F}, \tag{7}$$

where T and U are the eigenvalue matrices, whereas P and Q are the loading matrices of **X** and **Y**, respectively. It uses orthogonal matrix **T** and matrix **U** for regression modelling. The matrix U can be expressed using the following formula:

$$\mathbf{U} = \mathbf{TW}, \tag{8}$$

where **W** is the regression coefficient matrix (also known as the incidence matrix). The matrix **W** can be written as:

$$\mathbf{W} = (\mathbf{T}^{\mathrm{T}}\mathbf{T})^{-1}\mathbf{T}^{\mathrm{T}}\mathbf{Y}. \tag{9}$$

In general, the main steps of PLSR include (6) and (7) principal component decomposition of matrix **Y** and corresponding matrix **X** and (8) calculation of incidence matrix **W**.

In order to extract useful information from **X**, it is necessary to optimize the principal component of the PLSR model. In this work, the principal component is determined by k-fold cross validation method to obtain the optimal parameter.

c) Support Vector Regression

Support vector regression (SVR) is a nonlinear regression algorithm based on the principle of support vector machine (SVM). The main idea of SVR is to construct a hyperplane which makes the distance between the furthest sample point and hyperplane be the smallest. The function of hyperplane is:

$$y = w^T\varphi(x) + b, \tag{10}$$

where w is regression coefficient. In order to construct the hyperplane, the regression of SVR is described as solving the following equations:

$$\begin{cases} min(w, \xi_i, \xi_i^*, b)\frac{1}{2}||w||^2 + C\sum_{i=1}^{n}(\xi_i + \xi_i^*) \\ \quad s.t.\ |y_i - w(x_i + b)| \le \varepsilon + \xi_i^{(*)} \end{cases}, \tag{11}$$

where C is the penalty factor which represents the tolerance to the model fitting bias and directly affects the generalization ability of the model. ξ_i and ξ_i^* are slack variables, which represent the distance between

sample points and hyperplane. $\boldsymbol{\varepsilon}$ is the distance between support vector and hyperplane.[5,6] In the LIBS measurement, the characteristic spectral intensities show a linear relationship with the element concentrations. Thus LIBS has ability of quantitative analysis.[7–9] However, the relationship between the spectral matrix **X** and the concentration matrix **y** is generally nonlinear in the heterogeneous sample with high concentration, which is due to self-absorption effect.[10] It was reported that when the metal concentrations in solutions exceeded the threshold, the spectral intensities showed a nonlinear relationship with the concentrations.[11–13] Therefore, the multivariate regression algorithms are applied in order to obtain better quantitative analysis performance.[14–16] SVR uses the kernel function to map the matrix **X** into high-dimensional space and explores the linear relationship between **X** and **y**. In this work, the radial basis function (RBF) is chosen as the kernel function, and the detailed kernel function expression is shown in equation (12):

$$k(xi, xj) = exp(-\gamma||xi - xj||), \tag{12}$$

where γ determines the distribution of the raw dataset to the new feature space. In the present work, k-fold cross-validation combined with Grid search is used to optimize penalty factor.

C. Time-integrated spectra of the oil pollutants and the electrodes

The time-integrated spectra of oil pollutants plasmas in D-LIBS and in conventional laser-induced breakdown spectroscopy (C-LIBS), as well as the time-integrated spectra of electrode plasmas, are shown in Fig. S2. The electrodes in this work are made of cooper-tungsten and the concentration of oil pollutants is 200 mg/L. The spectra are normalized to its maximum emission intensity. Here, the W emission lines are only obtained from the electrode plasmas, which are marked in Fig. S2. From Fig. S2(b) and (c), Cr I 427.48 nm and Fe I 440.776 nm obtained from the oil pollutants plasma are influenced by W I 427.51 nm and W I 440.791 nm, respectively. And the rest of observed signals of metal elements in the experiments could be excluded from the contribution of trace element in the copper-tungsten electrode. Therefore, the enhancement ratios and LoDs of the rest of observed emission lines are investigated in this work.

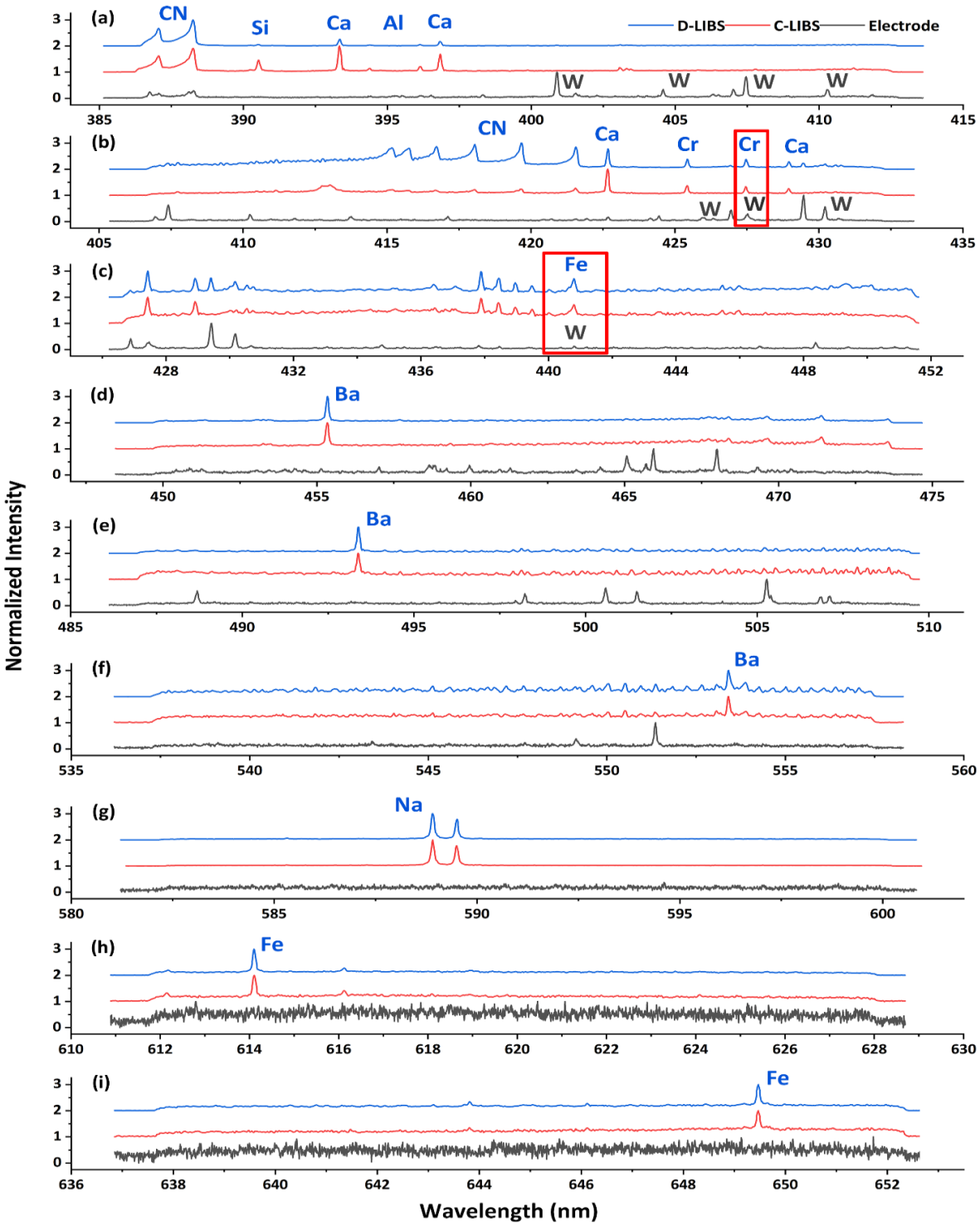

Figure S2. The time-integrated spectra of electrode and the time-integrated spectra of oil pollutants in C-LIBS and D-LIBS. The typical spectral lines are located in the wavelength range of (a) 385–415 nm, (b) 405–435 nm, (c) 428–452 nm, (d) 450–475 nm, (e) 485–510 nm, (f) 535–560 nm, (g) 580–600 nm, (h) 610–630 nm, and (i) 636–652 nm.

D. Spectra of the oil pollutants with and without wavelet transform de-noising (WTDN) in both C-LIBS and D-LIBS

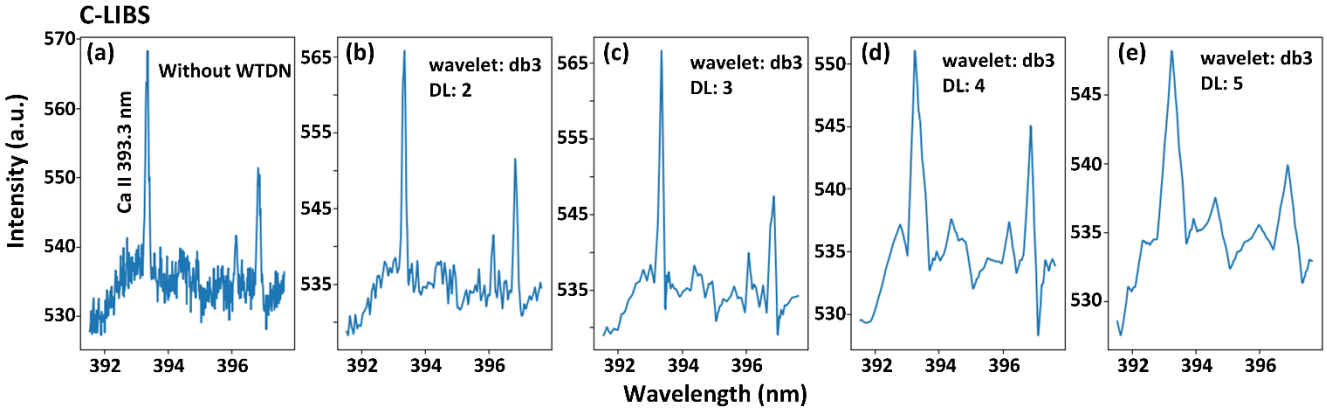

Figure S3. (a) The original time-integrated spectrum in C-LIBS. The time-integrated spectra in C-LIBS after using WTDN with the DL of (b) 2, (c) 3, (d) 4, and (e) 5. Note: DL means decomposition layer and the wavelet is fixed at db3.

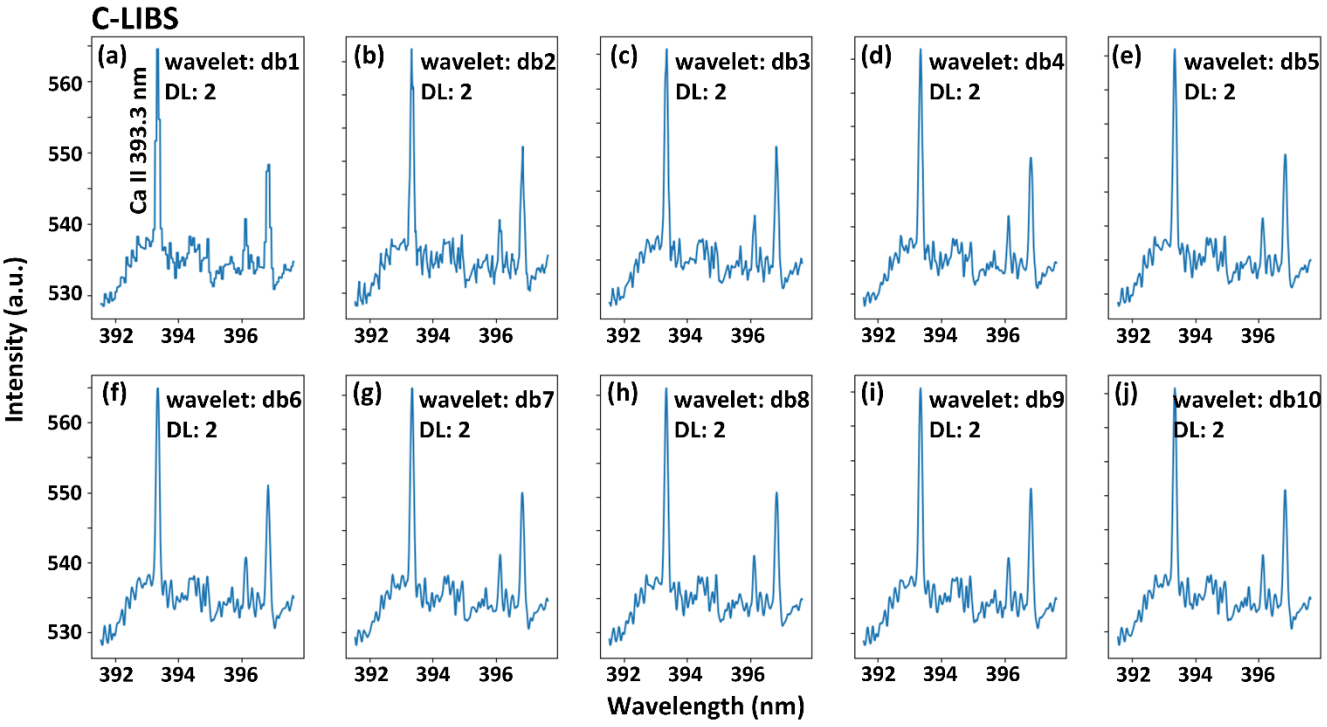

Figure S4. The time-integrated spectra in C-LIBS after using WTDN with the wavelet of (a) db1, (b) db2, (c) db3, (d) db4, (e) db5, (f) db6, (g) db7, (h) db8, (i) db9, and (j) db10. Note: DL means decomposition layer which is fixed at 2.

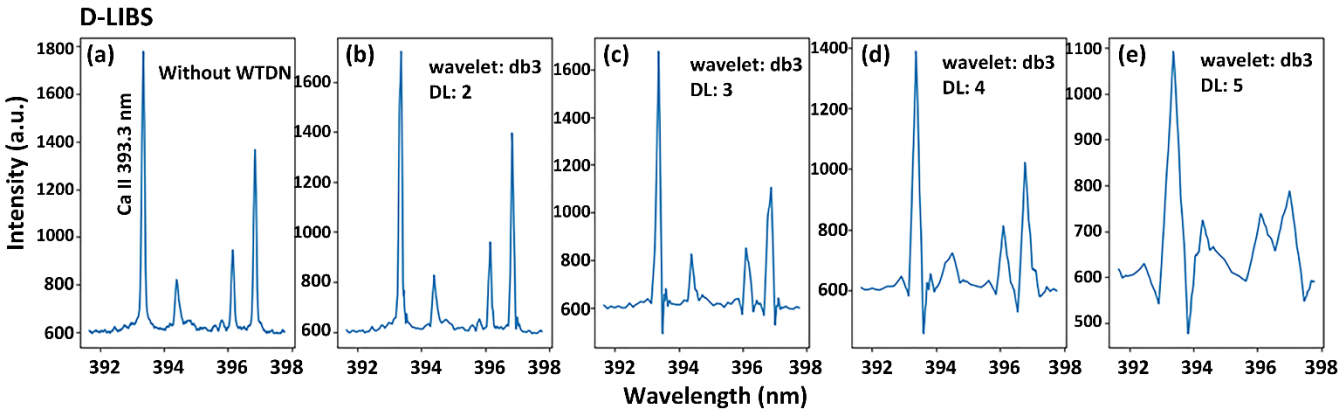

Figure S5. (a) The original time-integrated spectrum in D-LIBS. The time-integrated spectra in D-LIBS after using WTDN with the DL of (b) 2, (c) 3, (d) 4, and (e) 5. Note: DL means decomposition layer and the wavelet is fixed at db3.

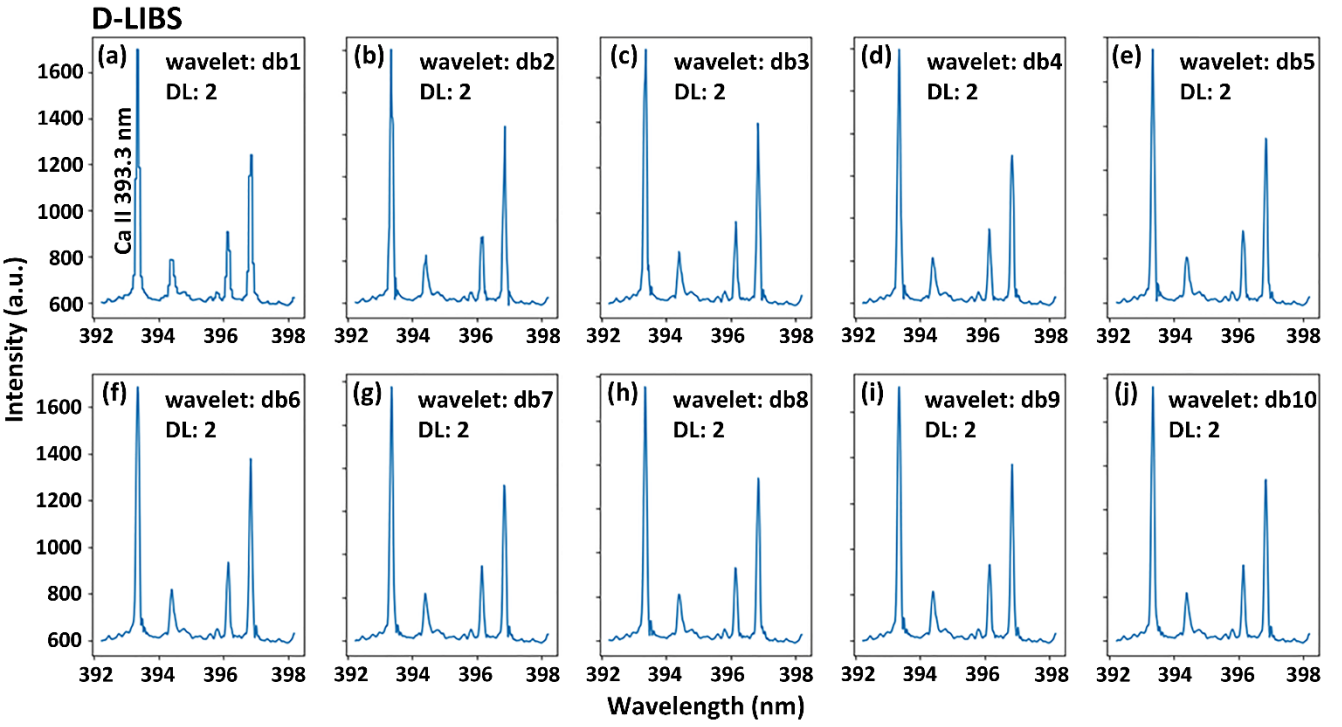

Figure S6. The time-integrated spectra in D-LIBS after using WTDN with the wavelet of (a) db1, (b) db2, (c) db3, (d) db4, (e) db5, (f) db6, (g) db7, (h) db8, (i) db9, and (j) db10. Note: DL means decomposition layer which is fixed at 2.

E. Comparison of the LoDs in this work and the reported literatures

Table S1. Comparison of the LoDs of metal elements in aqueous samples by various LIBS experimental methods.

Ref.	Approach	Method	LoDs of examined elements (mg/L)															
			Al	Ag	Ba	Ca	Cd	Cr	Cu	Fe	Li	Mg	Mn	Na	Ni	Pb	Sn	Zn
17	C-LIBS	Chelating resin enrichment					0.0036											
18	C-LIBS	Electrical-deposition					0.000528	0.000572	0.000083				0.000374			0.00051		0.005623
19	C-LIBS	Filter paper									10.5							
11	C-LIBS	Glass subplate		0.022			0.0446	0.0257	0.0128							0.0324		
11	MINAELIBS	Glass subplate		0.0034			0.0045	0.0035	0.0015							0.0035		
20	C-LIBS	Graphite enrichment					0.029	0.087	0.012						0.083	0.125		0.049
21	C-LIBS	Ion exchange membrane		0.43	0.13		0.21	0.13	0.0095						0.31	1.1		0.85
22	C-LIBS	LTS	0.01			0.01	1	0.1	0.01	0.01		0.01			0.01	10		1
23	C-LIBS	LTS by freeze					1.4	1.4	2.3	1.3		0.3				1.3		
24	C-LIBS	LTS by hydrogel-based-solidification	0.46					4.44	4.96									
25	C-LIBS	LTS by CaO					129	1.2								20		21
23	C-LIBS	LTS by quick-freeze	2											1				
26	C-LIBS	Wood slice subplate					0.59	0.034	0.029				0.036			0.074		
27	C-LIBS	PVA subplate		0.001			5	0.016	0.008						1	1		
28	LIBS-LIF	Wood slice subplate							0.0036									
29	SCLIBS	Aluminum electrode enrichment					0.0031									0.0012		0.0017
29	SCLIBS	Graphite enrichment					0.062	0.033	0.00353						0.044	0.83		0.18
30	SCLIBS	Graphite enrichment					0.0031	0.0122	0.0048						0.0343	0.0326		0.0361
31	SELIBS	Filter paper					0.038	0.1	0.04							0.054		
31	SELIBS	Without filter paper					0.061	0.037	0.064							0.047		
32	C-LIBS	Isolated droplet	5.2			0.4					0.3	1.9	7.2	2.2				

		generator																	
33	C-LIBS	Liquid jet												0.23					
34	C-LIBS	Liquid jet				0.6							3	10	0.08				
35	C-LIBS	Liquid jet							19										
36	C-LIBS	Liquid jet						30											
37	C-LIBS	Liquid surface														18			
23	C-LIBS	Liquid surface					7.1	10.5	9.6	10.5		0.9					12.5		
38	C-LIBS	Nebulization			1.5	0.4		5.8	8.8	14	0.2	0.16	2.7	1.6			40		6.2
39	C-LIBS	PTFE subplate	10			0.3		10	7	30		1		0.5	20		100	100	120
40	C-LIBS	Underwater			4.4	2.7						31.7	10.5						
41	C-LIBS	Underwater			6.8	0.13	500				0.013			0.0075			1.25		
42	C-LIBS	Underwater									0.17								
43	C-LIBS	Underwater				54					5		85						
44	C-LIBS	Underwater				0.94					0.00006								
45	C-LIBS	Underwater				2.46													
46	C-LIBS	Underwater										0.21							
35	DPLIBS	Liquid jet							12								13		
47	DPLIBS	Underwater	20			0.8					0.006	100		0.014					
48	DPLIBS	Underwater										1.4		0.4					
49	DPLIBS	Underwater						0.92				0.034	0.39						
50	DPLIBS	Underwater							2										
51	MHASLIBS[g]	MHAS				0.85	1.9			6.13	0.09	0.29	0.58	0.67					
52	MGCLIBS	MGC				0.98					0.13	3.31		0.18					
52	MGCLIBS	Without MGC				1.14					0.15	6.71		0.11					
53	C-LIBS	Nebulization							1.78	1.85		0.242	0.233	0.00596			21.7		0.596
54	C-LIBS	Nebulization	6.47			1.83	43.99	6.49	1.99			1.85		0.45			13.6		41.64

MINAELIBS: metal-chelate induced nanoparticle aggregation enhanced LIBS; LTS: liquid to solid; MHASLIBS: micro-hole array sprayer-assisted LIBS; MGCLIBS: micro-gas column LIBS.

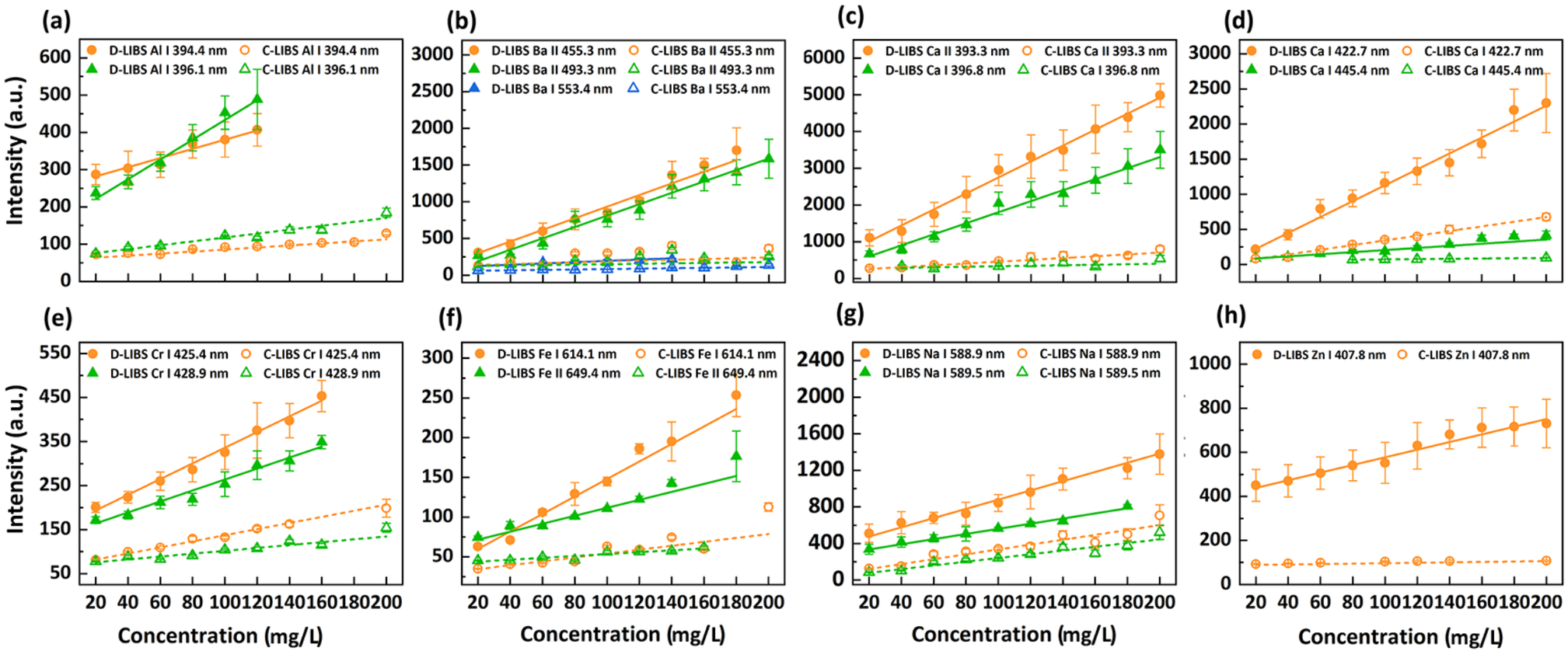

Fig. S7. The calibration curves of metal elements in wear oil in C-LIBS and D-LIBS. The metal elements are (a) Al, (b) Ba, (c,d) Ca, (e) Cr, (f) Fe, (g) Na, and (h) Zn. Each point in calibration curves corresponds to an average of 20 measurements at different locations of one prepared sample and the error bars denote the standard deviations of 20 measurements

Table S2. Comparison of the LoDs of metal elements in oil sample in this work and reported literatures.

Method	Sample	LoDs of examined elements (mg/L)							Ref.
		Al	Ba	Ca	Cr	Fe	Na	Zn	
D-LIBS, Si subplate	Oil pollutants	2.5 (I 396.1 nm)	0.7 (II 455.3 nm)	0.3 (II 393.3 nm)	3.5 (I 425.4 nm)	5.7 (I 614.1 nm)	1.1 (I 588.9 nm)	3.3 (I 407.8 nm)	This work
C-LIBS, Si subplate	Oil pollutants	12.9 (I 396.1 nm)	8.7 (II 455.3 nm)	2.0 (I 422.7 nm)	7.3 (I 425.4 nm)	19.0 (I 614.1 nm)	2.5 (I 588.9 nm)	79 (I 407.8 nm)	This work
C-LIBS, St. Surf.	Engine oil	35 (II 309.3 nm)	6.5 (II 455.3 nm)	6.2 (II 393.3 nm)			24 (I 588.9 nm)	11.4 (II 202.6 nm)	55
C-LIBS, Jets	Engine oil	15 (II 309.3 nm)	1.4 (II 455.3 nm)	0.4 (II 393.3 nm)	43 (I 425.4 nm)	20 (II 259.9 nm)	8 (I 588.9 nm)	11 (II 202.6 nm)	55
C-LIBS, FP	Engine oil	7 (II 309.3 nm)			29 (I 425.4 nm)	4 (II 259.9 nm)		5 (II 202.6 nm)	56
C-LIBS, Al subplate	Engine oil				10.59 (I 360.5 nm)	3.73 (II 259.9 nm)			57
C-LIBS, glass subplate	Engine oil				1.5 (II 284.3 nm)	3 (II 259.9 nm)			58
C-LIBS, Al subplate	Wear oil				8.11 (I 360.5 nm)	2.05 (II 259.9 nm)			59
C-LIBS, PTFE	Wear oil	10 (I 396.1 nm)		0.3 (II 393.3 nm)	20 (I 425.4 nm)	20 (I 371.9 nm)	0.7 (I 588.9 nm)	130 (I 334.5 nm)	39
C-LIBS, Si subplate	Wear oil				0.082 (I 425.4 nm)			3.9 (I 213.8 nm)	60
DP-LIBS FP	Engine oil	4 (II 309.3 nm)			12 (I 425.4 nm)	3 (II 259.9 nm)		2 (II 202.6 nm)	56

St. Surf: Static surfaces; FP: filter paper; DPLIBS: dual-pulse LIBS; PTFE: polytetrafluoroethylene.

Originating in the 1960s, LIBS has been used to analyze solid, gas, and liquid, due to its unique advantages, such as real time, in-situ, rapid, and simultaneous multielement detection. As for aqueous sample detection, LIBS technique is currently being investigated by several research groups for rapid identification and quantitative analysis of liquid samples, such as sea water, freshwater, bulk water, wastewater, potable water, and so on. The LoDs of metal elements in aqueous samples by various LIBS experimental methods are listed in Table S1. Commonly, the simplest method is directly detecting laser-induced plasmas underwater or on the static liquid surface. Underwater LIBS was employed for the quantitative analysis of dissolved metals in high-pressure CO_2-water solutions by Goueguel *et al*. [40] The LoDs for Mg, Ca, Ba, and Mg were found to be 31.7 mg/L, 2.5 mg/L, 4.4 mg/L, and 10.5 mg/L, where the pressure of water was 10 bars. Marion *et al*. [43] quantitative analyzed the metal elements in high-pressure bulk aqueous solutions. The LoDs for Ca, Li, and Mg were calculated to be 54 mg/L, 5 mg/L, and 85 mg/L, respectively. Leonard *et al*. [37] utilized a Nd:YAG laser operating at 60 mJ/pulse to focus onto the surface of the liquid and the LoD for Ni was calculated to be 18.0 mg/L. However, these approaches suffer from the plasma quenching and instability of liquid surface, and further reduce the intensity strength and analysis sensitivity. Considering that, researchers designed a series of liquid sample storage devices to improve the LIBS analysis performance. Ho *et al.* [33] designed a vertical liquid jet about 12 mm downstream from a flow cell and the LoD for Na was determined to be 0.23 mg/L, where the laser wavelength was 193 nm and the laser fluence was 3.3 J/cm^2. Aras *et al.* [54] designed and optimized a sample introduction system based on ultrasonic nebulization of metal silts in aqueous samples for LIBS. The LoDs for Cu, Fe, Mg, Mn, Na, Pb, and Zn were calculated to be 1.78 mg/L, 1.85 mg/L, 0.242 mg/L, 0.233 mg/L, 5.96 ng/mL, 21.7 mg/L, and 0.596 mg/L. Jiang *et al.* [52] introduced a specially designed micro-gas column assistance system to generate a 1.28 mm diameter stable micro-gas column in situ underwater and the laser pulses were focused on the gas-liquid interface of the column to improve LIBS spectral signal of metal elements in water sample. The LoDs for Mg, Ca Sr, Na, K, and Li were all less than 1 mg/L. A stable micro-hole array sprayer-assisted LIBS method for liquid sample analysis was discussed by Sheng *et al*. [51] The LoDs for Na, Ca, Mg, and K were 0.67 mg/L, 0.29 mg/L, 0.85 mg/L, and 6.18 mg/L. However, the spectral intensities and LoDs for trace elements are still undesirable. Considering a higher spectral intensity could be obtained in solid sample analysis, researchers transfer the target from liquid state into solid state. Electrode enrichment and graphite enrichment methods were applied for liquid detection. Some research groups obtained excellent analysis sensitivity. The LoDs for metal element were at ppb level even at ppt level [17,18,20,26,29]. Nevertheless, these methods need longtime sample preparation, which goes against the original intention of LIBS technique for rapid detection. Moreover, the enrichment behaviors of elements in the complex extraction process would be varied depending on the species and valence state of the elements, resulting in the limited analysis of some elements [61]. Hence, in order to meet rapid and real time measurement and obtain strong spectral intensity, double pulse LIBS (DP-LIBS) was developed for liquid sample detection [35,47–50]. In DP-LIBS, the LoDs for Li and Na were as low as 6 ng/mL and 14 ng/mL, respectively [47]. Nevertheless, the utilization of two lasers not only raises the cost, but also increases the difficulty of device integration.

In industrial fields, such as chemical plants, oil refinery, machinery factories, vehicles, ships, and aircraft manufacturing enterprises, there exist massive emissions of waste gasoline, engine oil, lubricating oil, and petroleum refining residue. It was reported that these industrial emissions were accidentally and carelessly discharged into the lakes, rivers, and oceans, resulting in the formation of a large area of oil pollution throughout the world. This oil pollution not only causes tremendous hazard to the natural environment that humans closely depend on, but also undermines the sustainable development of the ecological environment. Thus, the rapid and real-time quantitative analysis of trace elements in high-viscosity oil pollutants is

also of great significance for tracing the source of pollutant elements and crucial to the subsequent promulgation and implementation of reasonable prevention and governance measures. Fichet *et al.* [39] quantitatively analyzed the trace elements in wear oil by C-LIBS, and the LoDs for Al, Ca, Cr, Fe, Na, Zn were determined to be 10 mg/L, 0.3 mg/L, 20 mg/L, 20 mg/L, 0.7 mg/L, and 130 mg/L, respectively. The analysis sensitivities of trace elements in oil samples are still not desirable. DP-LIBS [56] is also utilized by some researchers. However, due to the disadvantages of DP-LIBS, a low-cost, handy, and real-time LIBS technique with high sensitivity is in urgent need for quantitative analysis of trace elements.

To fill this gap, we propose a method of D-LIBS combining with WTDN for trace elemental quantitative analysis. This method we proposed can obtain experimental results rapidly and real-time, which does not need complex experimental apparatus and longtime sample preparation. In the experiment, about μL oil pollutants is taken out and tiled it onto the Si subplate which is pure and clean. The thickness of liquid layer should be as thin as possible which is at μm level. The big advantage is that the thinner layer can efficiently reduce matrix effect and self-absorption effect [62]. In the main body, we comparatively investigate the C-LIBS and D-LIBS quantitative analysis performance of metal elements in oil pollutants. First, we induce plasmas from oil pollutants with various concentrations in C-LIBS and the LoDs for Al, Ba, Ca, Cr, Fe, Na, and Zn are determined to be 12.9 mg/L, 8.7 mg/L, 2.0 mg/L, 7.3 mg/L, 19.0 mg/L, 2.5 mg/L and 79 mg/L, respectively, by calibration curve model. The LoDs for metal elements in the similar oil samples from literatures are also listed in Table S2. It follows from Table S2 that the obtained LoDs for trace elements by C-LIBS in this work are located at the similar or same level as other experiments in the reported literatures.

In order to further improve the analysis sensitivity of LIBS, we introduce the discharge assisted equipment into laser induced plasma. The schematic diagram of experiment setup is shown in the main body (Figure 1). The principle of D-LIBS is that the electric energy is deposited into the plasma and the particles in the plasmas are reheated and the excitation/ionization is enhanced accordingly. Thus, a significant signal increase in D-LIBS is observed in comparison to C-LIBS. The signal intensities can be increased by one to two orders of magnitude. Besides, WTDN is also utilized in order to decrease the noise in measurement. Here, we did not directly compare the performance in our D-LIBS for oil pollutants detection and the performance in other experimental schemes which are in the previous reports. It is because that the difference of experiment conditions (i.e., differences from sample state, photoelectric detector, laser, spectrometer, and so on) can significantly affect LIBS quantitative analysis performance. In this work, we utilized the hybrid method of D-LIBS combining with WTDN for oil pollutants detection and compared to the results in C-LIBS. The results show that the signal intensities and analysis sensitivity are improved obviously. The enhancement ratios of CN emission lines intensities exceed 20-fold, and the trace elements signal intensities are increased 10-fold. And the SNR are also increased by one order of magnitude. As for analysis sensitivity, the LoDs are lowered to 1/2–1/24 of the original level. The LoDs for Al, Ba, Ca, Cr, Fe, Na, and Zn are determined to be 2.5 mg/L, 0.7 mg/L, 0.3 mg/L, 3.5 mg/L, 5.7 mg/L, 1.1 mg/L, and 3.3 mg/L, respectively. Thus, it is found that the analysis sensitivity of this hybrid method is comparable to its counterparts, such as DP-LIBS. In DP-LIBS, the LoDs for Al (II 309.3 nm), Cr (I 425.4 nm), Fe (II 259.9 nm), and Zn (II 202.6 nm) in engine oil were respectively examined to be 4 mg/L, 12 mg/L, 3 mg/L, and 2 mg/L by Yaroshchyk *et al.* [56], where the laser pulse for ablation was 170 mJ, the laser pulse for reheating was 95 mJ, and the delay time between the two laser pulses was 1 μs. Further comparison indicates that for the same elements in the similar oil products, the LoDs in our work are located at the same level as those in DP-LIBS. But for some typical elements, such as Ba and Ca, the LoDs are reduced to sub-ppm level. With the advantage of relatively low energy consumption (50 mJ laser pulse energy and 40 mJ discharge energy in our work) and simple and convenient experimental arrangement, the hybrid method has a

better performance in improvement of the analysis sensitivity for oil pollutants. Thus, we claim that the method of D-LIBS combining with WTDN is an alternative, economical, and reliable method for rapid and real-time quantitative analysis of trace metal elements with high-sensitivity in oil pollutants. By virtue of these merits, this hybrid method shows its great potential in various industrial applications, including chemical plants and oil refinery.

References

1 T. Yuan, Z. Wang, Z. Li, W. Ni and J. Liu, *Anal. Chim. Acta*, 2014, **807**, 29–35.
2 Y. Ding, W. Zhang, X. Zhao, L. Zhang and F. Yan, *J. Anal. At. Spectrom.*, 2020, **35**, 1131–1138.
3 X. Zhang, N. Li, C. Yan, J. Zeng, T. Zhang and H. Li, *J. Anal. At. Spectrom.*, 2020, **35**, 403–413.
4 R. Rosipal and N. Krämer, in *Subspace, Latent Structure and Feature Selection*, eds. C. Saunders, M. Grobelnik, S. Gunn and J. Shawe-Taylor, Springer Berlin Heidelberg, Berlin, Heidelberg, 2006, vol. 3940, pp. 34–51.
5 N. C. Dingari, I. Barman, A. K. Myakalwar, S. P. Tewari and M. Kumar Gundawar, *Anal. Chem.*, 2012, **84**, 2686–2694.
6 L. Song, W. Huang, X. Han and J. Mazumder, *IEEE Trans. Ind. Electron.*, 2017, **64**, 633–642.
7 M. Cui, H. Guo, Y. Chi, L. Tan, C. Yao, D. Zhang and Y. Deguchi, *Spectrochim. Acta Part B At. Spectrosc.*, 2022, **191**, 106398.
8 M. Fahad, A. Shahzad, S. Ali and K. H. Shah, *Appl. Opt.*, 2021, **60**, 5110.
9 A. Ciucci, M. Corsi, V. Palleschi, S. Rastelli, A. Salvetti and E. Tognoni, *Appl. Spectrosc.*, 1999, **53**, 960–964.
10 Y. Zhang, M. Dong, L. Cheng, L. Wei, J. Cai and J. Lu, *J. Anal. At. Spectrom.*, 2020, **35**, 810–818.
11 X. Liu, Q. Lin, Y. Tian, W. Liao, T. Yang, C. Qian, T. Zhang and Y. Duan, *J. Anal. At. Spectrom.*, 2020, **35**, 188–197.
12 C. Wu, D. X. Sun, M. G. Su, Y. P. Yin, W. W. Han, Q. F. Lu and C. Z. Dong, *J. Anal. At. Spectrom.*, 2019, **34**, 1478–1484.
13 F. Hilbk-Kortenbruck, R. Noll, P. Wintjens, H. Falk and C. Becker, *Spectrochim. Acta Part B At. Spectrosc.*, 2001, **56**, 933–945.
14 J. M. Andrade, G. Cristoforetti, S. Legnaioli, G. Lorenzetti, V. Palleschi and A. A. Shaltout, *Spectrochim. Acta Part B At. Spectrosc.*, 2010, **65**, 658–663.
15 G. Guo, G. Niu, Q. Shi, Q. Lin, D. Tian and Y. Duan, *Anal. Methods*, 2019, **11**, 3006–3013.
16 C. Niu, X. Cheng, T. Zhang, X. Wang, B. He, W. Zhang, Y. Feng, J. Bai and H. Li, *Anal. Chem.*, 2021, **93**, 2281–2290.
17 H. Tian, L. Jiao and D. Dong, *Sci. Rep.*, 2019, **9**, 10443.
18 Z. Chen, H. Li, F. Zhao and R. Li, *J. Anal. At. Spectrom.*, 2008, **23**, 871.
19 Y. He, X. Wang, S. Guo, A. Li, X. Xu, N. Wazir, C. Ding, T. Lu, L. Xie, M. Zhang, Y. Hao, W. Guo and R. Liu, *Appl. Opt.*, 2019, **58**, 422.
20 L. Fang, N. Zhao, M. Ma, D. Meng, Y. Jia, X. Huang, W. Liu and J. Liu, *Plasma Sci Technol*, 2019, **21**, 034002.
21 N. E. Schmidt and S. R. Goode, *Appl. Spectrosc.*, 2002, **56**, 370–374.
22 R. L. Vander Wal, T. M. Ticich, J. R. West and P. A. Householder, *Appl. Spectrosc.*, 1999, **53**, 1226–1236.
23 H. Sobral, R. Sanginés and A. Trujillo-Vázquez, *Spectrochim. Acta Part B At. Spectrosc.*, 2012, **78**, 62–66.
24 Q. Lin, F. Bian, Z. Wei, S. Wang and Y. Duan, *J. Anal. At. Spectrom.*, 2017, **32**, 1412–1419.
25 D. M. Díaz Pace, C. A. D'Angelo, D. Bertuccelli and G. Bertuccelli, *Spectrochim. Acta Part B At. Spectrosc.*, 2006, **61**, 929–933.
26 Z. Chen, H. Li, M. Liu and R. Li, *Spectrochim. Acta Part B At. Spectrosc.*, 2008, **63**, 64–68.
27 Q. Lin, X. Han, J. Wang, Z. Wei, K. Liu and Y. Duan, *J. Anal. At. Spectrom.*, 2016, **31**, 1622–1630.
28 Y. R. Wang, J. Kang, Y. Q. Chen and R. H. Li, *J. Appl. Spectrosc.*, 2019, **86**, 353–359.
29 D. Meng, N. Zhao, Y. Wang, M. Ma, L. Fang, Y. Gu, Y. Jia and J. Liu, *Spectrochim. Acta Part B At. Spectrosc.*, 2017, **137**, 39–45.
30 N. J. Zhao, D. S. Meng, Y. Jia, M. J. Ma, L. Fang, J. G. Liu and W. Q. Liu, *Opt. Express*, 2019, **27**, A495.
31 X. Yang, R. Yi, X. Li, Z. Cui, Y. Lu, Z. Hao, J. Huang, Z. Zhou, G. Yao and W. Huang, *Opt. Express*, 2018, **26**, 30456.
32 H. A. Archontaki and S. R. Crouch, *Appl. Spectrosc.*, 1988, **42**, 741–746.
33 W. F. Ho, C. W. Ng and N. H. Cheung, *Appl. Spectrosc.*, 1997, **51**, 87–91.
34 O. Samek, D. C. S. Beddows, J. Kaiser, S. V. Kukhlevsky, M. Liska, H. H. Telle and A. J. Whitehouse, *Opt. Eng.*, 2000, **39**, 2248.
35 K. Skočovská, J. Novotný, D. Prochazka, P. Pořízka, K. Novotný and J. Kaiser, *Rev. Sci. Instrum.*, 2016, **87**, 043116.
36 N. K. Rai and A. K. Rai, *J. Hazard. Mater.*, 2008, **150**, 835–838.
37 L. M. Berman and P. J. Wolf, *Appl. Spectrosc.*, 1998, **52**, 438–443.
38 A. A. Bol'shakov, S. J. Pandey, X. Mao and C. Liu, *Spectrochim. Acta Part B At. Spectrosc.*, 2021, **179**, 106094.
39 P. Fichet, P. Mauchien, J.-F. Wagner and C. Moulin, *Anal. Chim. Acta*, 2001, **429**, 269–278.
40 C. L. Goueguel, C. R. Bhatt, J. C. Jain, C. L. Lopano and D. L. McIntyre, *Opt. Laser Technol.*, 2018, **108**, 53–58.
41 R. Knopp, F. J. Scherbaum and J. I. Kim, *Fresenius J. Anal. Chem.*, 1996, **355**, 16–20.
42 B. Thornton, T. Takahashi, T. Sato, T. Sakka, A. Tamura, A. Matsumoto, T. Nozaki, T. Ohki and K. Ohki, *Deep Sea Res. Part Oceanogr. Res. Pap.*, 2015, **95**, 20–36.
43 M. Lawrence-Snyder, J. Scaffidi, S. M. Angel, A. P. M. Michel and A. D. Chave, *Appl. Spectrosc.*, 2006, **60**, 786–790.
44 C. Goueguel, D. L. McIntyre, J. Jain, A. K. Karamalidis and C. Carson, *Appl. Opt.*, 2015, **54**, 6071.
45 Y. Tian, S. Hou, L. Wang, X. Duan, B. Xue, Y. Lu, J. Guo and Y. Li, *Anal. Chem.*, 2019, **91**, 13970–13977.
46 V. Lazic, F. Colao, R. Fantoni and V. Spizzicchino, *Spectrochim. Acta Part B At. Spectrosc.*, 2005, **60**, 1002–1013.

47 D. A. Cremers, L. J. Radziemski and T. R. Loree, *Appl. Spectrosc.*, 1984, **38**, 721–729.
48 A. D. Giacomo, M. Dell'Aglio, F. Colao, R. Fantoni and V. Lazic, *Appl. Surf. Sci.*, 2005, **247**, 157–162.
49 V. Lazic, S. Jovicevic, R. Fantoni and F. Colao, *Spectrochim. Acta Part B At. Spectrosc.*, 2007, **62**, 1433–1442.
50 Y. Yu, W. Zhou and X. Su, *Opt. Commun.*, 2014, **333**, 62–66.
51 P. Sheng, L. Jiang, M. Sui and S. Zhong, *Spectrochim. Acta Part B At. Spectrosc.*, 2019, **154**, 1–9.
52 L. Jiang, M. Sui, Y. Fan, H. Su, Y. Xue and S. Zhong, *Spectrochim. Acta Part B At. Spectrosc.*, 2021, **177**, 106065.
53 S. Zhong, R. Zheng, Y. Lu, K. Cheng and J. Xiu, *Plasma Sci. Technol.*, 2015, **17**, 979–984.
54 N. Aras, S. Ü. Yeşiller, D. A. Ateş and Ş. Yalçın, *Spectrochim. Acta Part B At. Spectrosc.*, 2012, **74–75**, 87–94.
55 P. Yaroshchyk, R. J. S. Morrison, D. Body and B. L. Chadwick, *Spectrochim. Acta Part B At. Spectrosc.*, 2005, **60**, 986–992.
56 P. Yaroshchyk, R. J. S. Morrison, D. Body and B. L. Chadwick, *Spectrochim. Acta Part B At. Spectrosc.*, 2005, **60**, 1482–1485.
57 J. Xiu, L. Dong, Y. Liu and J. Li, *J. Appl. Spectrosc.*, 2019, **86**, 43–49.
58 L. Zheng, F. Cao, J. Xiu, X. Bai, V. Motto-Ros, N. Gilon, H. Zeng and J. Yu, *Spectrochim. Acta Part B At. Spectrosc.*, 2014, **99**, 1–8.
59 J. Xiu, V. Motto-Ros, G. Panczer, R. Zheng and J. Yu, *Spectrochim. Acta Part B At. Spectrosc.*, 2014, **91**, 24–30.
60 M. Vinić, E. Aruffo, F. Andreoli, M. Ivković and V. Lazic, *Spectrochim. Acta Part B At. Spectrosc.*, 2020, **164**, 105765.
61 M. Wu, X. Wang, G. Niu, Z. Zhao, R. Zheng, Z. Liu, Z. Zhao and Y. Duan, *Anal. Chem.*, 2021, **93**, 10196–10203.
62 J. Xiu, L. Dong, H. Qin, Y. Liu and J. Yu, *Appl. Spectrosc.*, 2016, **70**, 2016–2024.